Journal of Colloid and Interface Science 537 (2019) 569–578

Contents lists available at ScienceDirect

Journal of Colloid and Interface Science

journal homepage: www.elsevier.com/locate/jcis

Regular Article

KOH activation of wax gourd-derived carbon materials with high porosity and heteroatom content for aqueous or all-solid-state supercapacitors

Dan Yu, Yushuang Ma, Mingfeng Chen, Xiaoping Dong *

Department of Chemistry, Zhejiang Sci-Tech University, 928 Second Avenue, Xiasha Higher Education Zone, Hangzhou 310018, China

GRAPHICAL ABSTRACT

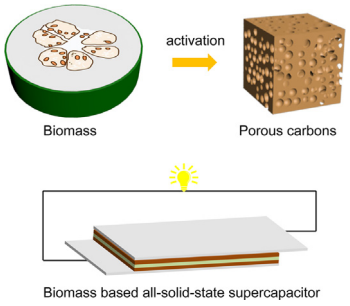

ARTICLE INFO

Article history:
Received 17 September 2018
Revised 9 November 2018
Accepted 16 November 2018
Available online 17 November 2018

Keywords:
Biomass
Wax gourd
Porous carbon
All-solid-state supercapacitor

ABSTRACT

Biomass precursors with natural porous structure and multifarious heteroatoms are desirably sustainable precursors for synthesis of carbon materials for energy and environmental applications. Herein, we reported wax gourd based porous carbons (WGPCs) with developed micro/mesoporous structures *via* potassium hydroxide (KOH) chemical activation. The optimized material that is denoted as WGPC-4 exhibits high specific surface area (2919 $m^2 g^{-1}$) with oxygen and nitrogen contents of 17.9 at.% and 1.0 at.%, respectively. In a three-electrode system, the WGPC-4 electrode presents high specific capacitance of 333 F g^{-1} at current density of 1 A g^{-1}. Meanwhile, the assembled symmetrical cell using aqueous electrolyte (0.5 M Na_2SO_4) has high specific capacitance (167 F g^{-1} at 1 A g^{-1}), stable cycling characteristics (93% capacitance retaining after 5000 runs) and excellent energy density of 19.2 Wh kg^{-1}. Furthermore, these WGPC-4 electrodes were assembled into an all-solid-state supercapacitor using KOH/polyvinyl alcohol (PVA) gel as solid electrolyte, whose specific capacitance is 258 F g^{-1} at 1 A g^{-1}, retention at the 2500th run is 87% and energy density is 13.0 Wh kg^{-1} under a high power density. These materials with excellent structural characteristics are an ideal candidate for high-performance supercapacitors.

1. Introduction

As energy shortages and environmental pollution escalate, supercapacitor (SC) that is one of the most promising energy storage devices has received considerable attention on account of their high power density and long-term cycling stability, etc. [1,2]. In general, the performance of SCs chiefly relies on electrode materials, which mainly include carbonaceous materials with porous structures (electric double-layer capacitance, EDLC), conductive polymers and transition metal (TM) oxides or sulfides (pseudo-capacitance) [3–5]. Faradic pseudo-capacitance materials have

* Corresponding author.
E-mail address: xpdong@zstu.edu.cn (X. Dong).

https://doi.org/10.1016/j.jcis.2018.11.070
0021-9797/

high values of specific capacitance, whereas they suffer the poor recycling stability, low current density and small potential window that will drastically decrease their power densities and energy densities [4]. Additionally, the choice of electrolyte is limited for some pseudo-capacitance materials. For example, most of TM oxides and sulfides need alkaline electrolytes.

Contrarily, carbonaceous porous structures possessing developed porosity and large surface area are favorable for the electrolyte diffusion and accumulation of abundant charges on surface [4,6,7]. Moreover, the well conductivity of carbon skeleton promotes the electron transfer in active materials. As a result, the commercial SCs are mainly assembled using porous carbons as active materials of electrodes. However, the relatively low energy density of SCs is difficult to fulfill the ever-increasing demands [8,9]. Thus, the design of advanced carbon electrode materials with superior electrochemical performance is essentially desirable for satisfying the high requirement of the energy storage market.

Recently, biomass derived carbons have paid great attention because the raw materials are low cost, renewable, readily available, and environment-friendly [10]. Furthermore, biomass is rich in multifarious heteroatoms, such as oxygen (O), nitrogen (N), sulfur (S) and phosphorus (P) [10,11]. The heteroatomic functionalities in resultant carbons can contribute additional pseudo-capacitance, as well as strengthen the surface wettability and framework electro-conductivity, therefore improving energy storage performance of carbon materials [7,12,13]. Generally, biomass-derived porous carbons are facilely synthesized by simple carbonization and activation treatment under the biomass pyrolyzing temperature of 600–900 °C using various activation approaches. As one of the most common activating route, the KOH activation is beneficial to acquire high specific surface area and well-developed pore structure [10,14]. Up to now, numerous porous carbons have been reported by KOH activation of biomass raw materials, including soybean [10], poplar catkins [15], corncob [16], bagasse wastes [17], carrageenan [18], etc. For example, G. Lin et al. reported that nitrogen-doped porous carbon with high surface area of up to 1749 $m^2 g^{-1}$ was prepared by KOH activation of soybean with hierarchical micro-mesoporous structures at 800 °C [10]. H. Feng et al. produced a combined hydrothermal carbonization and chemical activation processes using bagasse wastes as the precursor to obtain hierarchical structured carbon with high specific capacitance of 320 F g^{-1} [17].

Besides electrode materials, electrolytes also have an important effect on the performance of SCs. Despite the fact that liquid electrolytes have superb wetting of electrode surfaces and good conductivity, the practical application is restricted due to the low ion selectivity, large device size and poor portability [19,20]. Not only can solid electrolytes surmount the persistent problems of liquid electrolytes, but also act as the electrode separators and the ionic conducting media [19]. In addition, solid-state electrolytes for SCs offer the benefits of flexibility, lightweight, good ionic conductivity, wide electrochemical window, environmentally benign nature and so on [20–22]. Due to these benefits, solid-state SCs have promising applications in flexible and portable electronics. For instance, Xu et al. reported a three-dimensional (3D) graphene hydrogel for the fabrication of solid-state flexible SCs, which showed a high capacitance of 186 F g^{-1} at 1 A g^{-1} [23]. Wang et al. reported N-doped porous carbon materials derived from urea-modified lignin with high specific capacitances of 306 F g^{-1} at 0.1 A g^{-1} in KOH/PVA solid electrolytes [21]. Li et al. reported one-step electrochemically expanded graphite foil for flexible all-solid SC with high rate performance and high areal capacitance (30.5 mF cm^{-2}) [24]. Gong et al. synthesized three-dimensional porous graphitic carbon from bamboo char, and the assembled solid-state symmetric SC in KOH/PVA electrolyte exhibited considerable synergetic energy-power output properties for practical applications [25].

To the best of our knowledge, wax gourd is a kind of long-season, fast-growing vegetable and consumed widely in some countries [26]. It is mainly composed of major water and minor polysaccharides, and should be a hopeful precursor for fabrication of rich porous structure materials. Herein we employed KOH to activate wax gourd to prepare porous carbon materials with plentiful heteroatoms, prominent micro/mesoporous structure and large specific surface area. The resultant porous carbon materials exhibited the excellent capacitance, good long-term durability and superior rate capacity in both KOH/PVA solid electrolyte and aqueous electrolytes.

2. Experimental section

2.1. Reagents and materials

Potassium hydroxide (KOH), hydrochloric acid (HCl), sodium sulfate (Na_2SO_4) and conductive acetylene black were supplied by Sinopharm Chemical Reagent Co., Ltd. Polyvinylidene fluoride binder (PVDF) and polyvinyl alcohol (PVA) were obtained from Aladdin Industrial Corporation. Nickel foam (average pore diameter about 0.25 mm) was purchased from Shenzhen Kejing Star Technology Co., Ltd. All the chemical reagents were of analytical reagent grade and were used without further purification. Deionized water was used in all of the processes.

2.2. Preparation of wax gourd derived porous carbons

After removal of the peel, soft pulp and seeds, the flesh of wax gourd was sliced into small cubes and then freeze-dried. Subsequently, the freeze-dried flesh of wax gourd was pre-carbonized in a tube furnace under N_2 circumstance at 500 °C for 2 h. The resultant carbonized sample was added into KOH solution with KOH/carbon mass ratio of 1–4 (see Table S1). By removal of water in 100 °C oven, the mixture was heated in the tube furnace at 800 °C and held for 1 h under N_2 atmosphere. The wax gourd derived porous carbon (WGPC) materials were finally obtained *via* repeatedly washing using 1 M HCl solution and deionized water until the pH of 7. The obtained samples were denoted as WGPC-*x*, where *x* is the KOH/carbon mass ratio.

2.3. Preparation of electrodes and symmetric all-solid-state SCs

The working electrodes were fabricated by coating the slurry containing active material (80 wt%), conductive acetylene black (5 wt%) and PVDF (15 wt%) on nickel foam (1 × 1 cm). The electrodes were dried at 100 °C for 10 h in an oven before being compressed under a pressure of 20 MPa.

Symmetric all-solid-state SCs were assembled using two nearly same electrodes and KOH/PVA electrolyte. The KOH/PVA gel electrolyte was fabricated as follow: 1 g PVA was dissolved in 10 mL deionized water under vigorous stirring at 85 °C for 2 h; when the solution became clear, 10 mL KOH solution (6 M) was tardily added under stirring; keeping stirring at 85 °C for another 30 min, we obtained a clear gel electrolyte [21]. Then, these two electrodes were immersed in KOH/PVA solid electrolyte and dried in a fume hood to remove the excess water [25]. Finally, the symmetric all-solid-state SC was prepared by compressing these two electrodes.

2.4. Characterizations

Morphology and structure of WGPC were observed using a scanning electron microscope (SEM, Quanta 250 FEG) equipped with an energy-dispersive X-ray spectrometer (EDS) and transmission electron microscopy (TEM, JEOL JEM-2100) with an accelerating voltage of 200 kV. X-ray diffraction (XRD) patterns were obtained by on an X-ray diffractometer (DX-2700, Dandong Haoyuan Instrument Co. Ltd., China). Raman spectrum was examined on a RenishawinVia Raman microscope (spot size: 1 μm, laser power: 50 W). X-ray photoelectron spectroscopy (XPS) was collected on a VG K-ALPHA instrument with a monochromatic Al Kα source. Porous structure of WGPCs was studied by nitrogen sorption technology at −196 °C on a Micromeritics ASAP 2020 analyzer (outgassing condition: 200 °C, 6 h). The specific surface area (S_{BET}) was measured using the Brunauer-Emmett-Teller (BET) method, the pore size distributions were estimated using density functional theory (DFT), and the total pore volume was calculated based on the single-point method at a relative pressure (P/P_0) of 0.99.

2.5. Electrochemical measurements

Three-electrode system measurements: 6 M KOH aqueous solution, Ag/AgCl electrode and Pt sheet electrode were respectively used as electrolyte solution, reference electrode and counter electrode. Electrochemical performance of WGPCs was examined on a CHI660E electrochemical working station (Chenhua, Shanghai, China). Cyclic voltammetry (CV) examinations were performed by a potential window of −1.1 to −0.1 V at scan rates of 50–500 mV s^{-1}. Galvanostatic charge/discharge (GCD) measurements were conducted at different current densities of 0.5–40 A g^{-1} in the same potential range, and the gravimetric specific capacitance C (F g^{-1}) was determined according to the following equation [10]:

$$C = \frac{I\Delta t}{m\Delta V}$$

where I (A) shows the discharge current, Δt (s) refers to the discharge time, m (g) represents the active mass of working electrode material, and ΔV (V) expresses the potential range.

Two-electrode system measurements: 0.5 M Na_2SO_4 aqueous solution and KOH/PVA gel were respectively employed as liquid and solid electrolytes. Electrochemical impedance spectrometry (EIS) was collected in the frequency range from 0.01 Hz to 100 kHz at the open circuit voltage with an AC amplitude of 5 mV. The gravimetric specific capacitance Cs (F g^{-1}) for a single electrode was reckoned as follow [10,14]:

$$Cs = \frac{4I\Delta t}{m\Delta V}$$

where I (A) is the charge/discharge current, Δt (s) is the discharge time, m (g) is the total mass of active material in two electrodes, and ΔV (V) is the voltage change removing the internal resistance (IR) drop. The energy density (E, Wh kg^{-1}) and power density (P, W kg^{-1}) were estimated on the basis of the following equations [21,22]:

$$E = \frac{1}{2}C\Delta V^2$$

$$P = \frac{E \times 3600}{\Delta t}$$

3. Results and discussion

3.1. Physicochemical properties of WGPCs

The synthetic procedure of WGPCs is schematically illustrated in Fig. 1. Wax gourd has the highest water content (> 95%) in vegetables that consists of cellulose, protein and other elements. After removal of abundant water in wax gourd by freeze-drying route, the residual with macroscopic 3D skeleton was pre-carbonized at 500 °C. The carbon framework was further chemically etched by KOH at 800 °C to introduce developed micro/mesoporosities.

Without the chemical activation by KOH, the carbonized sample displays irregular particle and bulky framework shape (Fig. 2a–c). According to the mechanism of KOH activation, the carbon mass will decrease due to the reaction of C and KOH at high temperature to release CO_2 gas [27]. Therefore abounding macroscopic large porosities were produced in the texture of the KOH activated WGPC material (Fig. 2d–f). Compared to the chunk of skeleton in inactivated sample, the skeleton thickness of WGPC significantly thins, which can be demonstrated by the comparison of these SEM images in Fig. 2c and f. The structure of sheet-like porous carbons in the SEM photograph of WGPC (Fig. 2f) was investigated by TEM observation, and these images are depicted in Fig. 2g–i. Numerous nanosize porosities were produced by the KOH chemical activation that can be clearly found in Fig. 2h. Disordered fringes in Fig. 2i indicate the low graphitization degree.

XRD and Raman spectroscopy technologies were used to further determine the graphitization level of WGPCs. Two broad and weak peaks located at ~21° and ~43° are observed in all these WGPCs samples, which belong to the (0 0 2) and (1 0 0) diffractions of graphite structure with a low crystalline level (Fig. 3a). Raman spectra (Fig. 3b) depict two characteristic bands of carbonaceous structures. The D-band at the wavenumber of ~1340 cm^{-1} is related to the defects and disorder in carbon, while the G-band reflects the graphitized carbon [28]. And thus, the intensity ratio of I_D/I_G can be applied to evaluate the degree of graphitization in carbon materials [29]. As listed in Fig. 3b, the calculated I_D/I_G values of WGPCs are 0.97–0.99, revealing a low graphitization level. This is consistent with the results of TEM and XRD.

Elemental compositions and their chemical environment in WGPC were analyzed by XPS technique. The survey spectra in Figs. 4a and S1 illustrate the presence of C, N, O and P elements, and their contents in WGPCs are listed in Table S2. Besides the dominant C composition, all WGPC samples have similar heteroa-

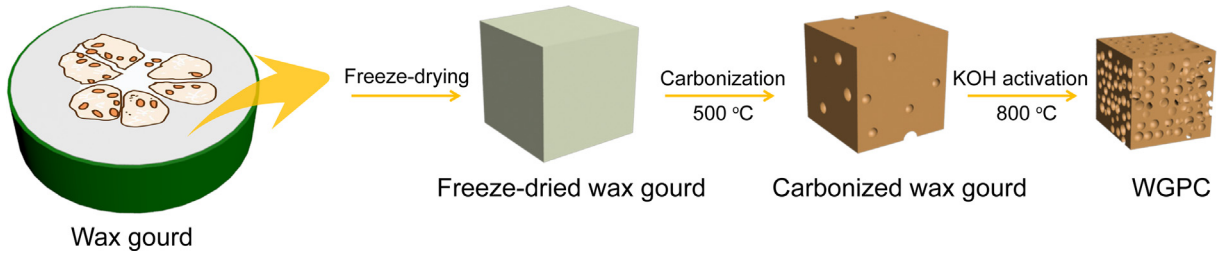

Fig. 1. Schematic illustration for the preparation of WGPCs from wax gourd.

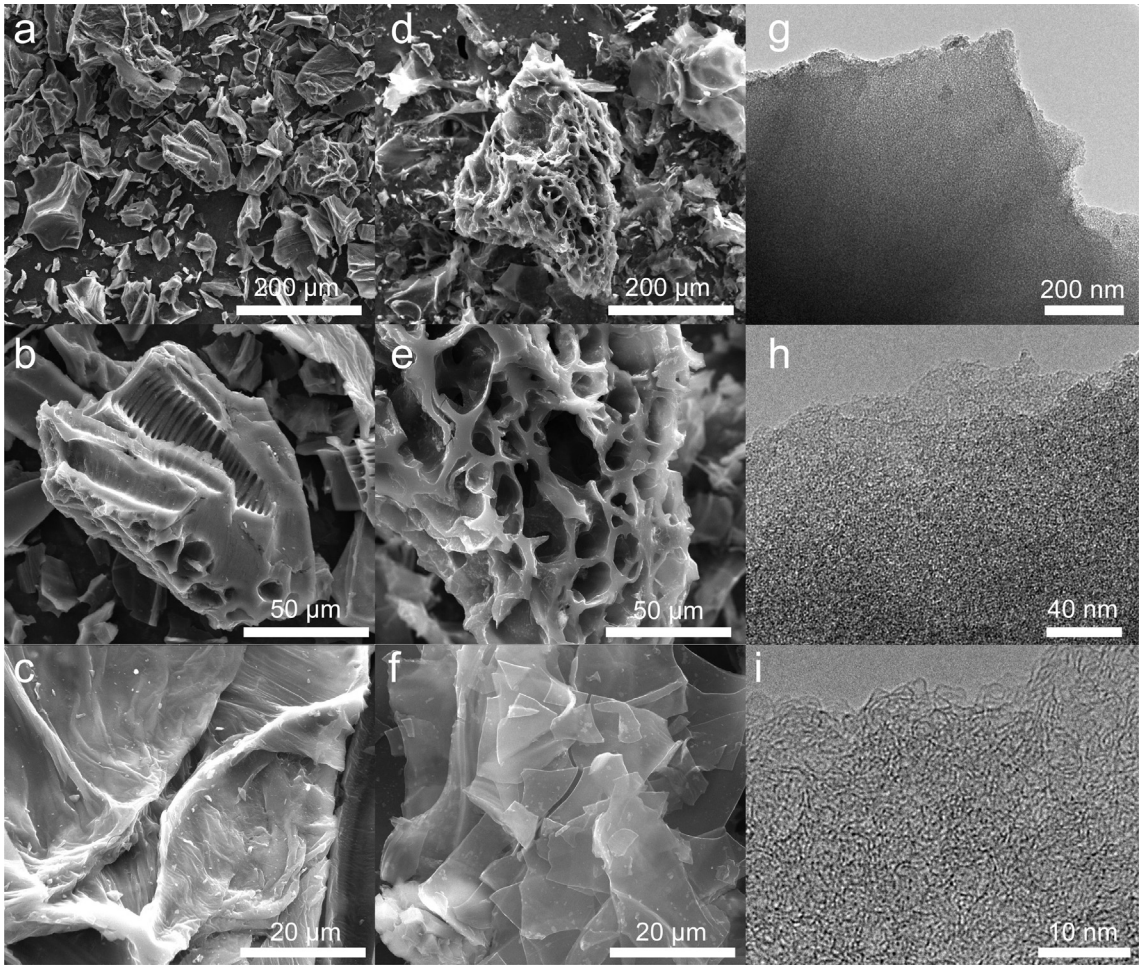

Fig. 2. SEM images of (a–c) the carbonized sample without the chemical activation by KOH and (d–f) WGPC-4; (g and h) TEM and (i) HRTEM images of WGPC-4.

tom percentages, 17–19 at.% for O, 1.9–0.9 at.% for N and 0.1–0.3 at.% for P, respectively. Due to the low concentrations of N and P, only C and O elemental mappings were obtained by SEM-EDS examination (Fig. S2). These heteroatoms play a crucial role in improvement of surface functionalities and electrochemical performance to electrode materials [30]. In particular, N compositions can not only contribute pseudocapacitance, but also enhance the conductivity of porous carbons [31,32]. The high resolution C 1s, O 1s and N 1s spectra are revealed in Fig. 4b–d. Four different types of carbon environments are found, and peaks at approximately 284.4, 285.6, 286.8 and 288.9 eV correspond to sp^2-C, sp^3-C, C—O and C═O groups, respectively [29,33]. The O 1s spectrum is fitted into three peaks. Among them, the main signal at 532.8 eV (O-II) is from C—OH phenol groups and/or C—O—C ether groups, and other two shoulder peaks at 531.7 eV (O-I) and 535.5 eV (O-III) are respectively ascribed to carbonyl groups and chemisorbed oxygen and/or water [13,34]. The oxygen groups especially carbonyl groups are electrochemically active, which can improve the electrochemical performance of the carbon material [13]. For the N 1s spectrum, it can also be deconvoluted into two peaks, corresponding to pyridinic-N (N-6, 398.3 eV) and quaternary-N (N-Q, 401.1 eV), respectively [29]. All present N atoms of the WGPC-4 sample mainly as the N-6 and N-Q. The N-6 atoms located at the periphery of graphitic layer can offer the pseudo-capacitance effect, while the N-Q atoms resided within the graphitic plane can improve the electronic conductivity of the carbon, which is beneficial for the supercapacitor performance [35].

Fig. 5 illustrates nitrogen adsorption-desorption isotherms of WGPCs and their corresponding pore size distributions. As shown in Fig. 5a, adsorbed volume of nitrogen rapidly increases at an extremely low relative pressure for WGPC-1 and WGPC-2 samples. These typical type-I isotherms imply the dominant micropore distributions in WGPC-1 and WGPC-2. It is obviously found in Fig. 5b where pore dimensions of WGPC-1 and WGPC-2 mainly locate in the range smaller than 2.0 nm. When enhance the KOH/C mass ratio to 3:1, the increase of adsorbed nitrogen prolongs to the relative pressure of 0.2, indicating the enlargement of pore size distribution. As seen in Fig. 5b, some mesopores with pore diameter of 2.0–3.0 nm were produced in WGPC-3 sample. As for WGPC-4, the more prominent effect of KOH chemical activation results in more developed porosity and the further expansion of pore size [36]. A continuous increase of adsorption amount with the relative pressure up to 0.4 is observed in the isotherm of WGPC-4. And its aspect is a bit like type-IV adsorption-desorption isotherm. This result suggests that mesopores have become dominant in WGPC-4 that is demonstrated by its pore size distribution. The calculated pore structure parameters are listed in Table 1. With increase of KOH/C mass ratio, the specific surface area and pore volume improve significantly from 1369 $m^2 g^{-1}$ and 0.62 $cm^3 g^{-1}$ for WGPC-1 to 2920 $m^2 g^{-1}$ and 1.84 $cm^3 g^{-1}$ for WGPC-4.

3.2. Electrochemical behaviors of WGPCs

WGPCs with developed porosity and heteroatom doped skeleton are expected to be ideal electrodes for supercapacitors. Accordingly, we investigated their electrochemical performance on a three-electrode configuration with typical 6 M KOH as electrolyte solution. Fig. 6a compares CV curves of different WGPCs in the

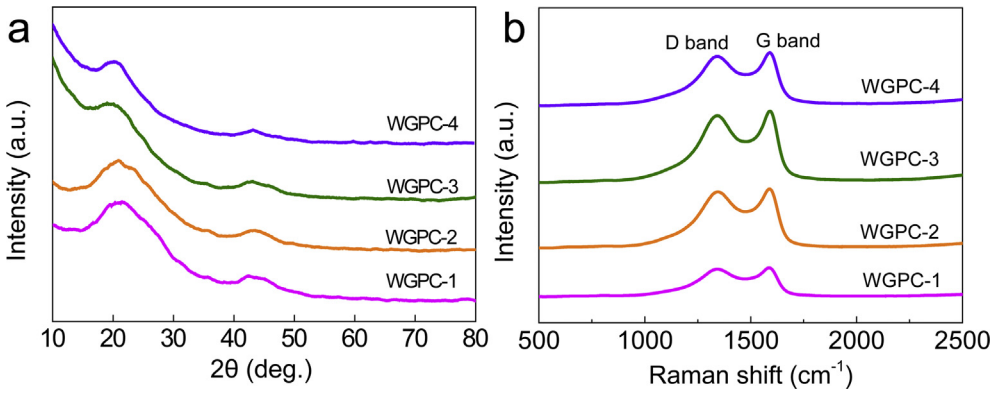

Fig. 3. (a) XRD patterns and (b) Raman spectra of WGPCs.

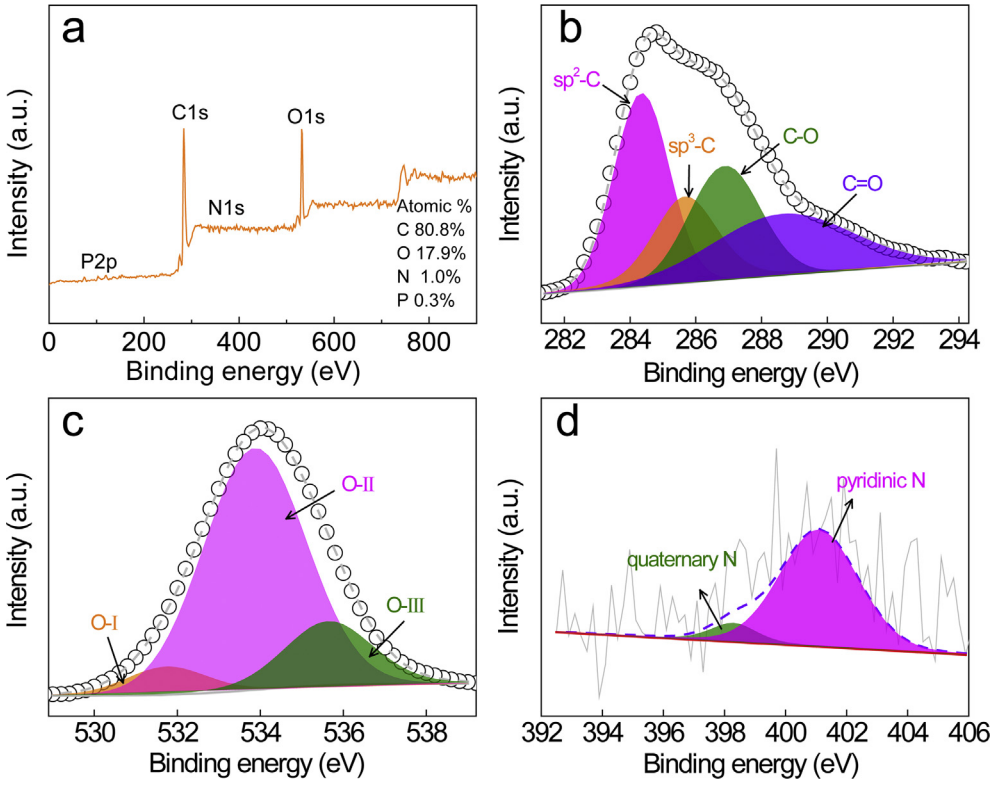

Fig. 4. XPS spectra of WGPC-4: (a) survey, (b) C 1s, (c) O 1s and (d) N 1s.

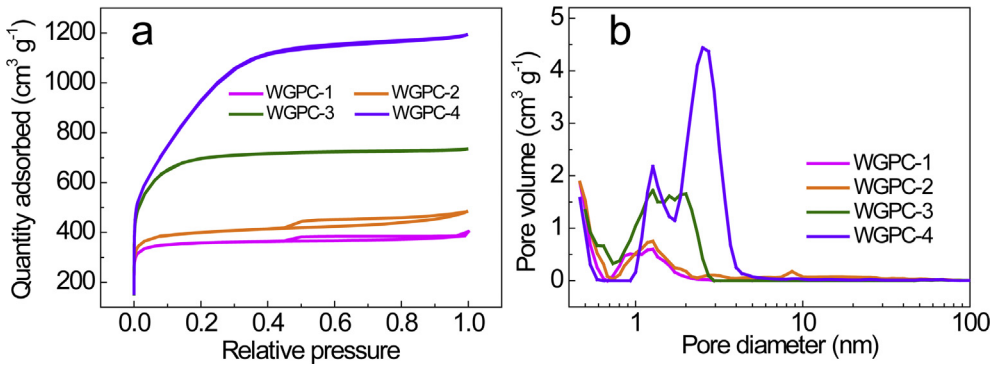

Fig. 5. (a) Nitrogen adsorption-desorption isotherms and (b) the corresponding pore size distributions of WGPCs.

Table 1
Textural parameters of WGPCs.

Sample	S_{BET}[a] ($m^2\ g^{-1}$)	S_{micro}[b] ($m^2\ g^{-1}$)	S_{meso}[c] ($m^2\ g^{-1}$)	V_{total}[d] ($cm^3\ g^{-1}$)	V_{micro}[e] ($cm^3\ g^{-1}$)	V_{meso}[f] ($cm^3\ g^{-1}$)	Error[g] (%)
WGPC-1	1368	1217	151	0.62	0.49	0.13	2.88
WGPC-2	1514	1267	247	0.75	0.51	0.24	2.79
WGPC-3	2544	1747	797	1.14	0.72	0.42	2.91
WGPC-4	2919	470	2449	1.84	0.36	1.48	2.48

[a] Specific surface area estimated using BET method.
[b] Micropore surface area calculated using the V-t plot method.
[c] Mesopore surface area: $S_{meso} = S_{BET} - S_{micro.}$
[d] Total pore volume calculated using single point method at $P/P_0 = 0.99$.
[e] Micropore pore volume calculated using the V-t plot method.
[f] Mesopore pore volume: $V_{meso} = V_{total} - V_{micro.}$
[g] Specific surface area error. The number of repeat experiments underlying error estimates is four times.

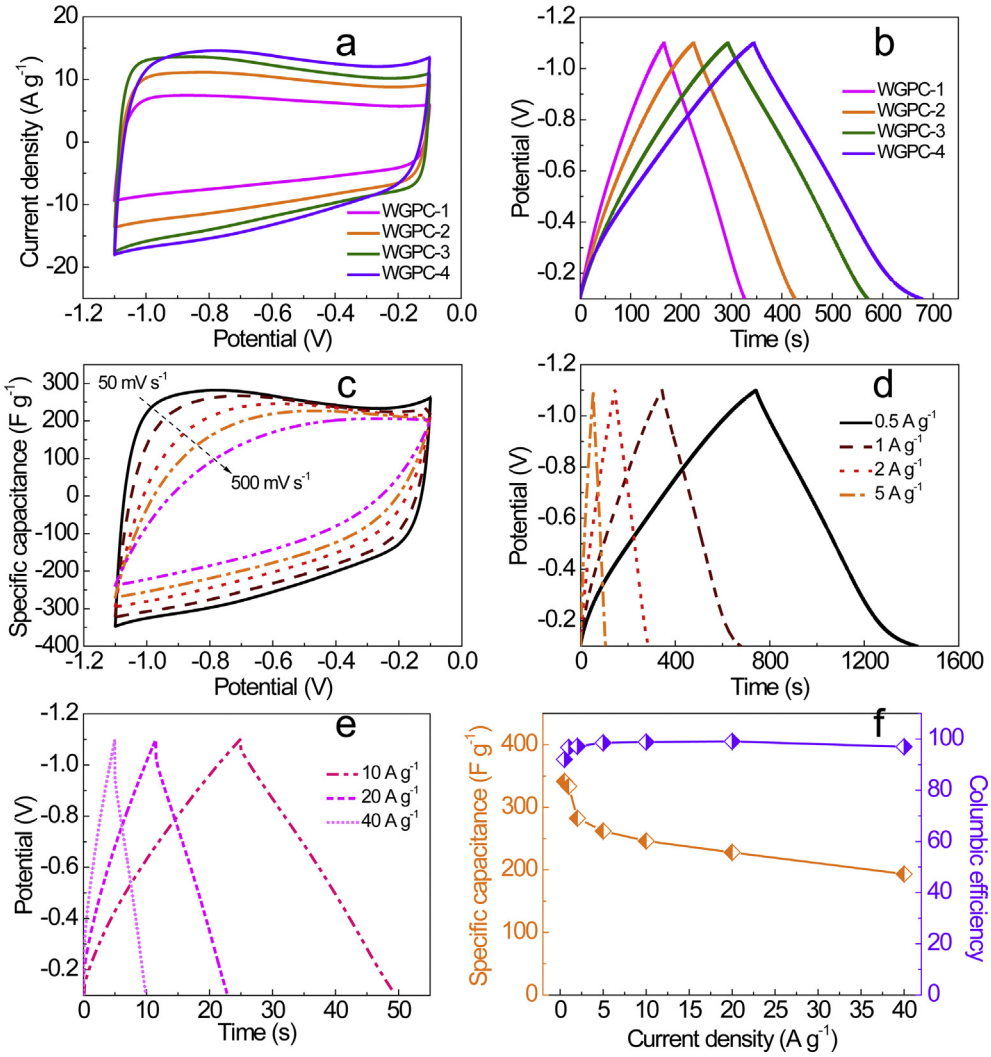

Fig. 6. (a) Electrochemical behavior in 6 M KOH using a three-electrode system: (a) CV curves (50 mV s^{-1}) and (b) GCD curves (1 A g^{-1}) of WGPCs; (c) CV curves at various scan rates, (d and e) GCD curves at different current densities and (f) the rate performance and Columbic efficiency of WGPC-4 electrode.

potential range of −1.1 to −0.1 V at a scan rate of 50 mV s^{-1}. Quasi-rectangular curve shapes indicate the typical behavior of EDLCs. It is clearly seen that WGPC-4 has the largest integral area of CV curve, demonstrating its highest specific capacitance. Additionally, we obtained similar outcome from the GCD experiment (Fig. 6b). Linear and symmetrical GCD curves at the current density of 1 A g^{-1} confirm that WGPCs have good electrochemical reversibility and high charge/discharge efficiency. Their corresponding specific capacitances calculated from the discharge branch are 160, 201, 277 and 333 F g^{-1} for WGPC-1, WGPC-2, WGPC-3 and WGPC-4, respectively. Due to the similar atomic compositions in various WGPCs (Table S2), the difference of specific capacitances may be attributed to their different porous structures. The specific capacitance of active materials is mainly determined by their available surface that electrolyte ions can be adsorbed on. In addition, the electrolyte diffusion in interior of electrodes is another vital

factor for the electrochemical performance of materials. Limited by the small channel size, the electrolyte transportation in micropores has big resistance. However, mesoporous channels can act as "highway" to promote the electrolyte diffusion and make them rapidly reach interior surface of electrodes [9,37]. Because the WGPC-4 sample has the most developed porosity with largest specific surface area and pore volume among these WGPCs, the highest specific capacitance was achieved by the WGPC-4 based electrode. Moreover, we compared the WGPC-4 sample with our previously reported heteroatom-free porous carbons that have similar porous structure to WGPSs [38–41]. The much higher specific capacitance of WGPC-4 demonstrates the promotion effect of heteroatoms on the electrochemical performance. This capacitance value is also comparable to or even better than those of the reported biomass based porous carbons (Table S3). The effect of activation temperature on electrochemical behavior is presented in Fig. S3 and Table S4. The CV curve of WGPC sample activated at 800 °C has the largest enclosed area and it meanwhile has the longest discharge time among these WGPC samples that were prepared under different temperatures. Additionally, we also compared the electrochemical behaviors of wax gourd based porous carbons using various activators (Fig. S4 and Table S5). The optimized WGPC-4 has better performance than the $ZnCl_2$ and K_2CO_3 activated carbons.

We further studied the electrochemical behavior of WGPC-4 electrode under various scanning rates or current densities. As displayed in Fig. 6c, the CV curves gradually change from rectangular to spindle-like with increasing the scanning rate from 50 to 500 mV s^{-1}, and the enclosed area also decrease step by step. It should be ascribed to the limited electrolyte diffusion in pores under high scanning rate [42]. GCD curves obtained by different current density are exhibited in Fig. 6d and e. The evaluated specific capacitance values (Fig. 6f) are 341, 333, 283, 262, 246, 228 and 193 F g^{-1} at current densities of 0.5, 1, 2, 5, 10, 20 and 40 A g^{-1}, respectively. Similarly, the transport rate of electrolyte ions is suppressed under the high current density that induces the capacitance gradually decreases as improving the current density, like other carbonaceous electrodes [10,43,44]. It is, nevertheless, that the WGPC-4 electrode still maintains a high specific capacitance ~200 F g^{-1} even at 40 A g^{-1}, implying that its good rate capability. Additionally, ~100% Columbic efficiency reveals the excellent electrochemical utilization of WGPC-4 (Fig. 6f).

3.3. WGPC based symmetrical SCs

To evaluate the practical viability of WGPC-4 as electrode materials, we further investigated its performance for symmetrical SCs in aqueous or solid electrolyte.

3.3.1. WGPC based aqueous SCs

The aqueous SC was assembled by two identical electrodes using 0.5 M Na_2SO_4 aqueous solution as electrolyte. The potential window (0–1.8 V) is determined in Fig. S5. Fig. 7a depicts CV curves of the symmetrical cell at various scan rates, and quasi-rectangle is maintained even at a high scan rate of 2000 mV s^{-1}, manifesting the superior transportability of electrons and ions in the cell. Moreover, the charge–discharge behavior of the aqueous SC was also tested at different current densities from 0.5 to 20 A g^{-1} (Figs. 7b and S6). The charge-discharge profiles show relatively symmetrical triangular shapes, and the internal resistance (IR) drop gradually increases with the increase of current density. Under the 20 A g^{-1} current density, the GCD curve show a ~0.2 IR drop. As seen in Fig. 7c, a high specific capacitance value of 172 F g^{-1} at 0.5 A g^{-1} is obtained. It still remains 159 F g^{-1} even when the current density increases to 20 A g^{-1} (90.5% of initial capacitance at 0.5 A g^{-1}), which suggests that this symmetrical aqueous SC has an excellent rate capability. At low current density, the columbic efficiency is relatively low. The incomplete discharge may be ascribed to some side reactions in the electrochemical redox process [45]. As increasing the current density, the electrochemical process is basically determined by the formation of the electrical double layer and accordingly, the columbic efficiency closes to

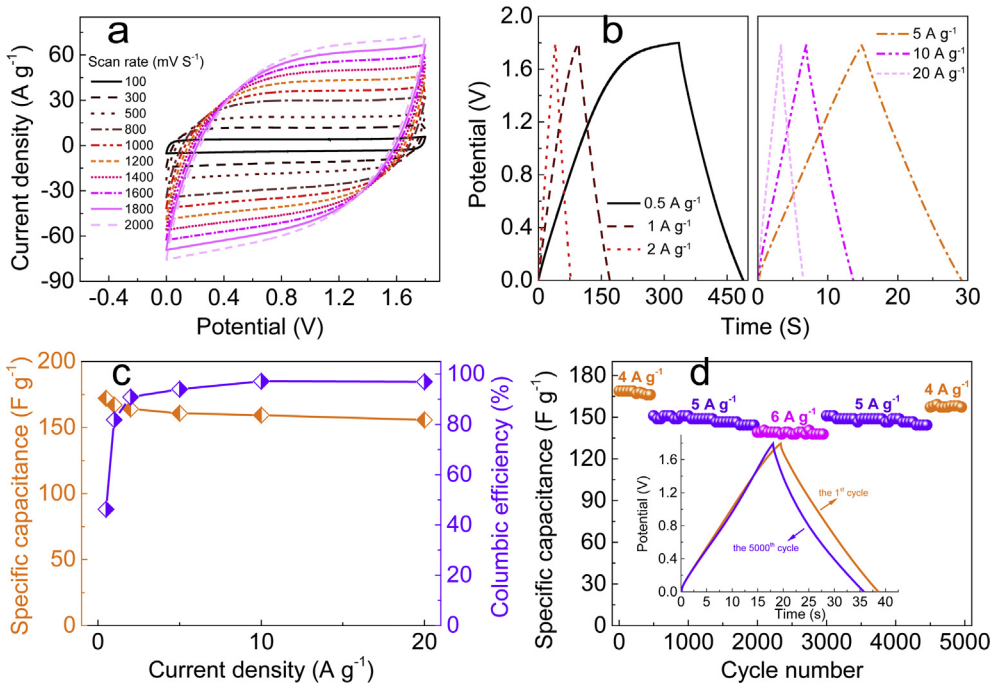

Fig. 7. Electrochemical behavior of WGPC-4 based symmetric SC in 0.5 M Na_2SO_4 aqueous electrolyte: (a) CV measurements at different scan rates in the potential range of 0–1.8 V; (b) GCD profiles at different current densities; (c) specific capacitances and Coulombic efficiency at various current densities; (d) The long-cycling stability at the current densities of 4, 5 and 6 A g^{-1}, and the inset is the GCD curves of the 1st and the 5000th cycle.

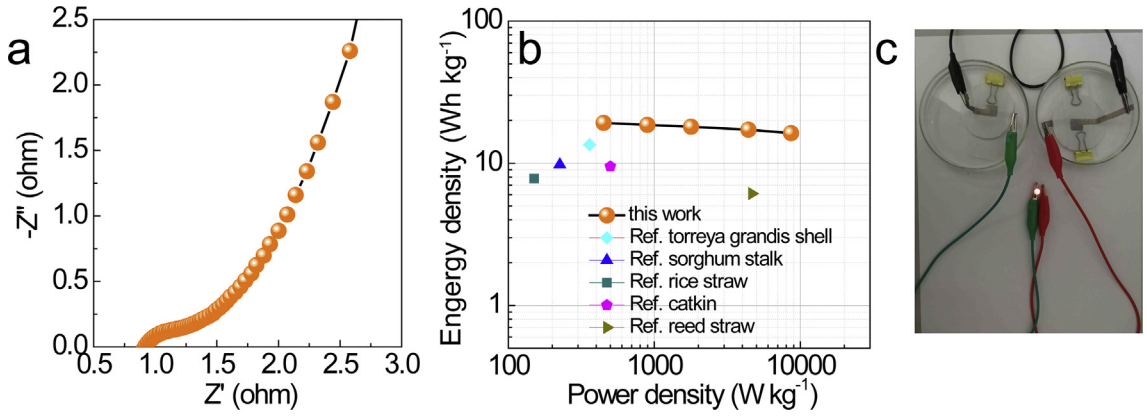

Fig. 8. (a) Nyquist plot (the inset is the equivalent circuit) and (b) Ragone plot of the WGPC-4 symmetric SC in 0.5 M Na_2SO_4 aqueous electrolytes. (c) A red LED was powered by the two WGPCs based symmetric supercapacitors in series. (For interpretation of the references to color in this figure legend, the reader is referred to the web version of this article.)

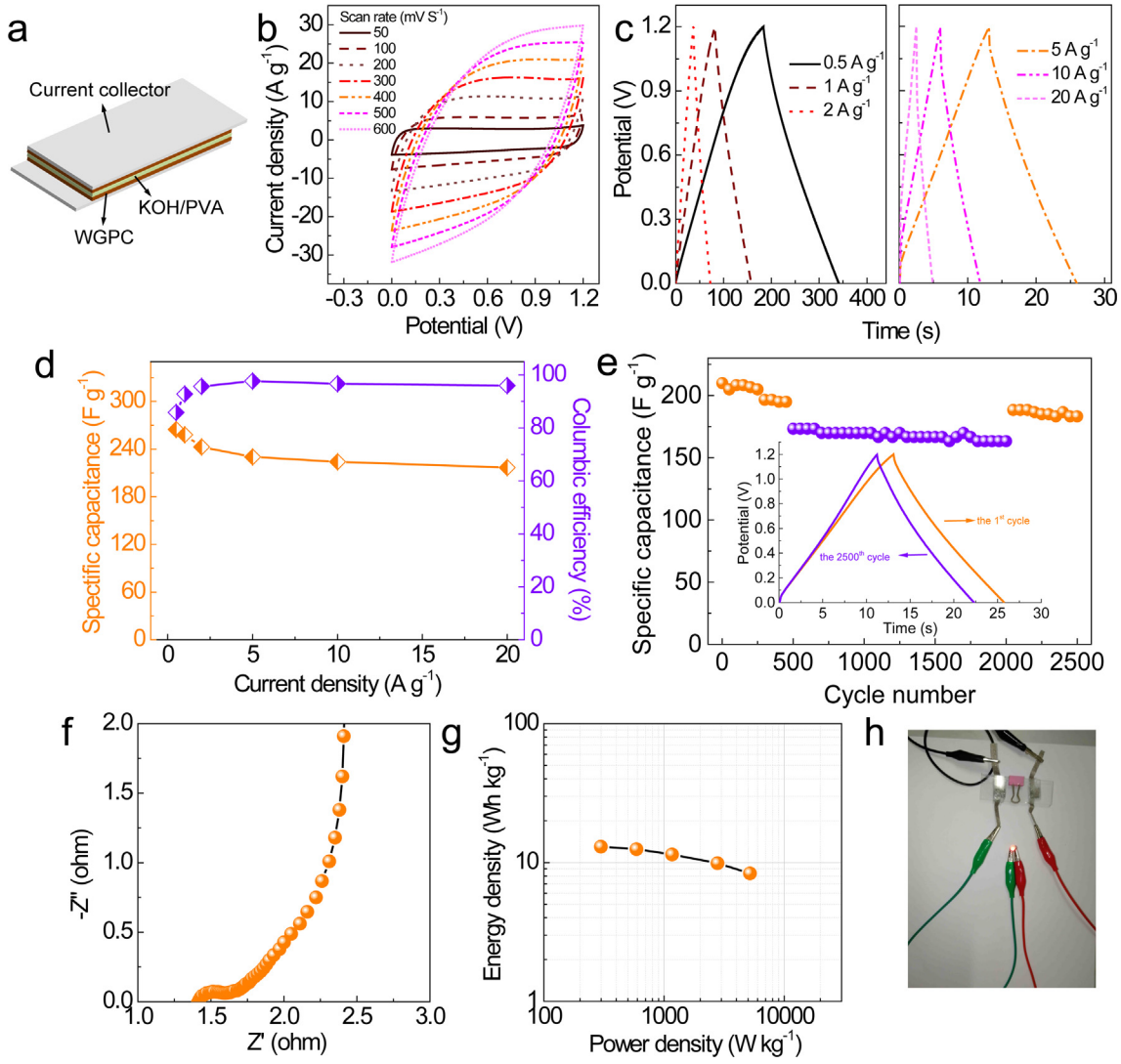

Fig. 9. Electrochemical performance of the WGPC-4 based all-solid-state symmetric SC: (a) Schematic illustration of the all-solid-state SC device; (b) CV curves at different scan rates; (c) GCD profiles at various current densities; (d) specific capacitances and Coulombic efficiency at various current densities; (e) The long-cycling stability at different current densities of 5 and 10 A g^{-1}, and the inset is the GCD curves of the 1st and the 2500th cycle; (f) Nyquist plot; (g) Ragone plot; (h) lighting a red LED. (For interpretation of the references to color in this figure legend, the reader is referred to the web version of this article.)

97% [46]. The cycling stability of this SC was evaluated by successive 5000 GCD tests under different current densities (Fig. 7d). 93% retention of initial capacitance at 4 A g^{-1} was kept after 5000 cycles, suggesting it good stability and reusability. The inset in Fig. 7d depicts the GCD curves of the 1st and the 5000th cycles. There is no difference in the voltage drop between the two curves,

reflecting that the IR of this aqueous SC didn't improve significantly after 5000 cycles.

Electrochemical impedance spectroscopy (EIS) is also a critical technique to study the electron/ion transport process, and the Nyquist plot of the symmetric aqueous cell is shown in Fig. 8a. In the low frequency region, the steep slope of the curve indicates an equivalent series resistance of ion diffusion and migration [9]. The intercept of the curve at the Z' axis is defined as solution resistance (Rs). The diameter of semicircle corresponds to the charge transfer resistance (Rct) at the electrode/electrolyte interface in high frequency region [47,48].

The inset is the fitted equivalent circuit that is consistent of five parts, where Rs is the solution resistance, Cdl is a double-layer capacitor, Rct is the charge transfer resistance, W is the Warburg impedance, and CPE (the constant phase element) is defined to cater for the deviation from ideal capacitor behavior [47]. The estimated values of Rs and Rct are respectively 0.92 and 0.24 Ω, suggesting a low internal resistance for this aqueous SC. The Ragone plot is presented in Fig. 8b. It is found that a maximum energy density of 19.2 Wh kg^{-1} is obtained at 448.5 W kg^{-1}, which still is retained as 16.3 Wh kg^{-1} at a high power density of 8625 W kg^{-1}. More importantly, the energy density is comparable to or even higher than most of the other biomass-derived carbons (see Table S6), such as sorghum stalk-derived carbon (9.77 Wh kg^{-1} at 225.35 W kg^{-1}) [49], Torreya grandis shell-derived carbon (13.5 Wh kg^{-1} at 360.1 W kg^{-1}) [41], catkin-derived carbon (9.5 Wh kg^{-1} at 500 W kg^{-1}) [50], reed straw-derived carbon (6.12 Wh kg^{-1} at 4660 W kg^{-1}) [51] and rice straw-derived carbon (7.8 Wh kg^{-1} at 150 W kg^{-1}) [52]. In summary, suitable pore structure, large specific surface area, moderate heteroatom dopants and low internal resistance of WGPC-4 based electrodes make clear such high energy and power densities. Fig. 8c displays a red light-emitting diode (LED) lit by two series connected aqueous cells in 0.5 M Na_2SO_4. This experiment further signifies the immense potential of WGPC material for high performance SCs.

3.3.2. WGPC based all-solid-state SCs

Fig. 9a exhibits the basic schematic illustration of the all-solid-state symmetric SC device that is constituted with two identical pieces of WGPC-4 electrodes using KOH/PVA solid electrolyte. As shown in Fig. S7, the potential window of this all-solid-state SC is optimized as 0–1.2 V. In this potential range, CV curves of all-solid-state SC present almost standard rectangular shape even though broadening the scan rate from 50 to 600 mV s^{-1} (Fig. 9b). The near-perfect triangular shape of GCD curves is revealed in Fig. 9c with current densities increasing from 1 to 20 A g^{-1}. As seen in Fig. S8, a relative big IR drop is presented under high current density, indicating its large internal resistance. The gravimetric capacitance reaches 265 F g^{-1} at the current density of 0.5 A g^{-1}. And the value of 258 F g^{-1} at 1 A g^{-1} is obviously higher than that of the previously reported all-solid-state carbonaceous SCs (Table S7). Fig. 9d plots the corresponding specific capacitance and columbic efficiency at various current densities. 81.9% retention of initial capacitance is achieved at the current density of 20 A g^{-1}. It is noted that the energy efficiencies of all-solid-state SC are 80–97% in the current density of 1–20 A g^{-1}, suggesting heat loss was produced during the charge/discharge process [21]. To evaluate the cycle stability of the all-solid-state SC, the continuous charge-discharge process was carried out at current densities of 5 and 10 A g^{-1} for 2500 cycles (Fig. 9e). Approximately 87% of specific capacitance is reserved, proving its excellent long-term cycling stability. Nyquist plot of the all-solid-state SC (Fig. 9f) depicts a little circular, demonstrating a quick charge transfer rate. From the EIS data, the Rs and Rct values are calculated as 1.42 and 0.15 Ω, respectively. It should be noted that the Rs of all-solid-state SC is greater than that of the aqueous SC, which can be attributed to the reason that the solid electrolyte is difficult to diffuse into the inner of electrodes [21,53]. The Ragone plot of this all-solid-state SC is illustrated in Fig. 9g. The largest energy density of 13.0 Wh kg^{-1} is brought out at the power density of 297.5 W kg^{-1} (current density of 0.5 A g^{-1}) in PVA/KOH solid electrolyte. This energy density is markedly higher than those previously reported porous carbon (see Table S7), including bamboo-derived carbon (6.68 Wh kg^{-1} at 100.2 W kg^{-1}) [25], camellia petal-derived porous carbon (6.5 Wh kg^{-1} at 270 W kg^{-1}) [54], and N-doped carbon nanofibers (5.9 Wh kg^{-1} at 1200 W kg^{-1}) [55]. Furthermore, a tandem device filled with KOH/PVA solid electrolyte is also capable to light a red LED.

4. Conclusions

In summary, heteroatoms doped porous carbon with excellent performance has been successfully synthesized from sustainable biomass precursor of wax gourd *via* carbonization and activation approach. The WGPC-4 possesses high specific surface area (up to 2920 m^2 g^{-1}) and abundant micro-mesoporous structure, which is beneficial to enhance the adsorption of electrolyte ions and promote their diffusion in electrode. It shows a superior specific capacitance of 333 F g^{-1} in 6 M KOH aqueous electrolyte under current density of 1 A g^{-1} in a three-electrode system. High electrochemical performance is also achieved by symmetric SCs both in aqueous electrolyte (0.5 M Na_2SO_4) and in KOH/PVA solid-state electrolyte. The aqueous SC has a specific capacitance of 167 F g^{-1} under current density of 1 A g^{-1}, and an excellent energy density of 16.3 Wh kg^{-1} at a high power density of 8625 W kg^{-1}. The all-solid-state SC possesses a large specific capacitance of 258 F g^{-1} at 1 A g^{-1}, and its energy density is 13.0 Wh kg^{-1} at a power density of 297.5 W kg^{-1}. We compared the electrochemical performance of WGPC-4 with the reported results in references both in three-electrode setups (Table S3) and in assembled SCs with aqueous (Table S6) or solid-state electrolytes (Table S7). Its performance is comparable to the reported carbon based SCs in references and even better than them. This investigation reveals that sustainable biomass sources are promising precursors to design novel porous carbons with developed hierarchical porosities, large accessible surface area and plentiful heteroatomic dopants for electrochemical energy storage applications. Furthermore, the residual of freeze-dried wax gourd has 3D inter-connected framework, and its derived carbons provide possibilities to fabricate binder-free and flexible devices.

Acknowledgements

This work was financially supported from the financial support from the Zhejiang Provincial Natural Science Foundation of China (No. LY17B010004) and the 521 talent project of ZSTU.

Appendix A. Supplementary material

Supplementary data to this article can be found online at https://doi.org/10.1016/j.jcis.2018.11.070.

References

[1] K. Xie, X. Qin, X. Wang, Y. Wang, H. Tao, Q. Wu, L. Yang, Z. Hu, Carbon nanocages as supercapacitor electrode materials, Adv. Mater. 24 (2012) 347–352.
[2] J. Ni, Y. Li, Carbon nanomaterials in different dimensions for electrochemical energy storage, Adv. Energy Mater. 6 (2016) 1600278.
[3] J. Wang, P. Nie, B. Ding, S. Dong, X. Hao, H. Dou, X. Zhang, Biomass derived carbon for energy storage devices, J. Mater. Chem. A 5 (2017) 2411–2428.
[4] G. Wang, L. Zhang, J. Zhang, A review of electrode materials for electrochemical supercapacitors, Chem. Soc. Rev. 41 (2012) 797–828.

[5] Z. Wu, L. Li, J. Yan, X. Zhang, Materials design and system construction for conventional and new-concept supercapacitors, Adv. Sci. 4 (2017) 1600382.
[6] D.W. Wang, F. Li, M. Liu, G.Q. Lu, H.M. Cheng, 3D aperiodic hierarchical porous graphitic carbon material for high-rate electrochemical capacitive energy storage, Angew. Chem. 120 (2008) 379–382.
[7] E. Frackowiak, Carbon materials for supercapacitor application, Phys. Chem. Chem. Phys. 9 (2007) 1774–1785.
[8] J. Deng, T. Xiong, F. Xu, M. Li, C. Han, Y. Gong, H. Wang, Y. Wang, Inspired by bread leavening: one-pot synthesis of hierarchically porous carbon for supercapacitors, Green Chem. 17 (2015) 4053–4060.
[9] N. Guo, M. Li, X. Sun, F. Wang, R. Yang, Enzymatic hydrolysis lignin derived hierarchical porous carbon for supercapacitors in ionic liquids with high power and energy densities, Green Chem. 19 (2017) 2595–2602.
[10] G. Lin, R. Ma, Y. Zhou, Q. Liu, X. Dong, J. Wang, KOH activation of biomass-derived nitrogen-doped carbons for supercapacitor and electrocatalytic oxygen reduction, Electrochim. Acta 261 (2018) 49–57.
[11] W. Wan, Q. Wang, L. Zhang, H.W. Liang, P. Chen, S.H. Yu, N-, P- and Fe-tridoped nanoporous carbon derived from plant biomass: an excellent oxygen reduction electrocatalyst for zinceair batteries, J. Mater. Chem. A 4 (2016) 8602–8609.
[12] B. Xua, D. Zheng, M. Jia, G. Cao, Y. Yang, Nitrogen-doped porous carbon simply prepared by pyrolyzing a nitrogen-containing organic salt for supercapacitors, Electrochim. Acta 98 (2013) 176–182.
[13] W. Yang, W. Yang, A. Song, L. Gao, L. Su, G. Shao, Supercapacitance of nitrogen-sulfur-oxygen co-doped 3D hierarchical porous carbon in aqueous and organic electrolyte, J. Power Sour. 359 (2017) 556–567.
[14] B. Wang, J. Qiu, H. Feng, E. Sakai, T. Komiyama, KOH-activated nitrogen doped porous carbon nanowires with superior performance in supercapacitors, Electrochim. Acta 190 (2016) 229–239.
[15] X.L. Su, M.Y. Cheng, L. Fu, J.H. Yang, X.C. Zheng, X.X. Guan, Superior supercapacitive performance of hollow activated carbon nanomesh with hierarchical structure derived from poplar catkins, J. Power Sour. 362 (2017) 27–38.
[16] D.B. Wang, Z. Geng, B. Li, C.M. Zhang, High performance electrode materials for electric double-layer capacitors based on biomass-derived activated carbons, Electrochim. Acta 173 (2015) 377–384.
[17] H.B. Feng, H. Hu, H.W. Dong, Y. Xiao, Y.J. Cai, B.F. Lei, Y.L. Liu, M.T. Zheng, Hierarchical structured carbon derived from bagasse wastes: a simple and efficient synthesis route and its improved electrochemical properties for high-performance supercapacitors, J. Power Sour. 302 (2016) 164–173.
[18] Y. Fan, X. Yang, B. Zhu, P.F. Liu, H.T. Lu, Micro-mesoporous carbon spheres derived from carrageenan as electrode material for supercapacitors, J. Power Sour. 268 (2014) 584–590.
[19] C. Zhong, Y. Deng, W. Hu, J. Qiao, L. Zhang, J. Zhang, A review of electrolyte materials and compositions for electrochemical supercapacitors, Chem. Soc. Rev. 44 (2015) 7484–7539.
[20] A. Manthiram, X. Yu, S. Wang, Lithium battery chemistries enabled by solid-state electrolytes, Nat. Rev. Mater. 2 (2017) 16103.
[21] K. Wang, M. Xu, Y. Gu, Z. Gu, Q.H. Fan, Symmetric supercapacitors using urea-modified lignin derived N-doped porous carbon as electrode materials in liquid and solid electrolytes, J. Power Sour. 332 (2016) 180–186.
[22] X. Xiao, T. Li, P. Yang, Y. Gao, H. Jin, W. Ni, W. Zhan, X. Zhang, Y. Cao, J. Zhong, L. Gong, W.C. Yen, W. Mai, J. Chen, K. Huo, Y.L. Chueh, Z.L. Wang, J. Zhou, Fiber-based all-solid-state flexible supercapacitors for self-powered systems, ACS Nano 6 (2012) 9200–9206.
[23] Y. Xu, Z. Lin, X. Huang, Y. Liu, Y. Huang, X. Duan, Flexible solid-state supercapacitors based on three-dimensional graphene hydrogel films, ACS Nano 7 (2013) 4042–4049.
[24] H.Y. Li, Y. Yu, L. Liu, L. Liu, Y. Wu, One-step electrochemically expanded graphite foil for flexible all-solid supercapacitor with high rate performance, Electrochim. Acta 228 (2017) 553–561.
[25] Y. Gong, D. Li, C. Luo, Q. Fu, C. Pan, Highly porous graphitic biomass carbon as advanced electrode materials for supercapacitors, Green Chem. 19 (2017) 4132–4140.
[26] M. Nakashima, Y. Shigekuni, T. Obi, M. Shiraishi, A. Miyamoto, H. Yamasaki, T. Etoh, S. Iwai, Nitric oxide-dependent hypotensive effects of wax gourd juice, J. Ethnopharmacol. 138 (2011) 404–407.
[27] J. Wang, S. Kaskel, KOH activation of carbon-based materials for energy storage, J. Mater. Chem. 22 (2012) 23710–23725.
[28] W. Yu, H. Wang, S. Liu, N. Mao, X. Liu, J. Shi, W. Liu, S. Chen, X. Wang, N, O-codoped hierarchical porous carbons derived from algae for high-capacity supercapacitors and battery anodes, J. Mater. Chem. A 4 (2016) 5973–5983.
[29] L. Peng, Y. Liang, H. Dong, H. Hu, X. Zhao, Y. Cai, Y. Xiao, Y. Liu, M. Zheng, Super-hierarchical porous carbons derived from mixed biomass wastes by a stepwise removal strategy for high-performance supercapacitors, J. Power Sour. 377 (2018) 151–160.
[30] J. Zhou, J. Lian, L. Hou, J. Zhang, H. Gou, M. Xia, Y. Zhao, T.A. Strobel, L. Tao, F. Gao, Ultrahigh volumetric capacitance and cyclic stability of fluorine and nitrogen co-doped carbon microspheres, Nat. Commun. 6 (2015) 8503.
[31] L.T. Song, Z.Y. Wu, H.W. Liang, F. Zhou, Z.Y. Yu, L. Xu, Z. Pan, S.H. Yu, Macroscopic-scale synthesis of nitrogen-doped carbon nanofiber aerogels by template-directed hydrothermal carbonization of nitrogen-containing carbohydrates, Nano Energy 19 (2016) 117–127.
[32] L.N. Han, X. Wei, Q.C. Zhu, S.M. Xu, K.X. Wang, J.S. Chen, Nitrogen-doped carbon nets with micro/mesoporous structures as electrodes for high-performance supercapacitors, J. Mater. Chem. A 4 (2016) 16698–16705.
[33] P. Hao, Z. Zhao, Y. Leng, J. Tian, Y. Sang, R.I. Boughton, C.P. Wong, H. Liu, B. Yang, Graphene-based nitrogen self-doped hierarchical porous carbon aerogels derived from chitosan for high performance supercapacitors, Nano Energy 15 (2015) 9–23.
[34] Y. Zhao, W. Ran, J. He, Y. Song, C. Zhang, D.B. Xiong, F. Gao, J. Wu, Y. Xia, Oxygen-rich hierarchical porous carbon derived from artemia cyst shells with superior electrochemical performance, ACS Appl. Mater. Interfaces 7 (2015) 1132–1139.
[35] S. Yu, N. Sun, L. Hu, L. Wang, Q. Zhu, Y. Guan, B. Xu, Self-template and self-activation synthesis of nitrogen-doped hierarchical porous carbon for supercapacitors, J. Power Sour. 405 (2018) 132–141.
[36] K. Kierzek, E. Frackowiak, G. Lota, G. Gryglewicz, J. Machnikowski, Electrochemical capacitors based on highly porous carbons prepared by KOH activation, Electrochim. Acta 49 (2004) 515–523.
[37] S. Dutta, A. Bhaumik, K.C.-W. Wu, Hierarchically porous carbon derived from polymers and biomass: effect of interconnected pores on energy applications, Energy Environ. Sci. 7 (2014) 3574–3592.
[38] B. Chang, Y. Wanga, K. Pei, S. Yang, X. Dong, $ZnCl_2$-activated porous carbon spheres with high surface area and superior mesoporous structure as an efficient supercapacitor electrode, RSC Adv. 4 (2014) 40546–40552.
[39] Y. Wang, B. Chang, D. Guan, X. Dong, Mesoporous activated carbon spheres derived from resorcinol-formaldehyde resin with high performance for supercapacitors, J. Solid State Electrochem. 6 (2015) 1783–1791.
[40] H. Xuan, Y. Wang, G. Lin, F. Wang, L. Zhou, X. Dong, Z. Chen, Air-assisted activation strategy for porous carbon spheres to give enhanced electrochemical performance, RSC Adv. 6 (2016) 15313–15319.
[41] H. Xuan, G. Lin, F. Wang, J. Liu, X. Dong, F. Xi, Preparation of biomass-activated porous carbons derived from torreya grandis shell for high-performance supercapacitor, J. Solid State Electrochem. 8 (2017) 2241–2249.
[42] A. Alabadi, X. Yang, Z. Dong, Z. Li, B. Tan, Nitrogen-doped activated carbons derived from a co-polymer for high supercapacitor performance, J. Mater. Chem. A 2 (2014) 11697–11705.
[43] Y. Bu, T. Sun, Y. Cai, L. Du, O. Zhuo, L. Yang, Q. Wu, X. Wang, Z. Hu, Compressing carbon nanocages by capillarity for optimizing porous structures toward ultrahigh-volumetric-performance supercapacitors, Adv. Mater. 29 (2017) 1700470.
[44] J. Xu, Z. Tan, W. Zeng, G. Chen, S. Wu, Y. Zhao, K. Ni, Z. Tao, M. Ikram, H. Ji, Y. Zhu, A hierarchical carbon derived from sponge-templated activation of graphene oxide for high-performance supercapacitor electrodes, Adv. Mater. 28 (2016) 5222–5228.
[45] D. Qu, H. Shi, Studies of activated carbons used in double-layer capacitors, J. Power Sour. 74 (1998) 99–107.
[46] N.S. Choi, Z. Chen, S.A. Freunberger, X. Ji, Y.K. Sun, K. Amine, G. Yushin, L.F. Nazar, J. Cho, P.G. Bruce, Challenges facing lithium batteries and electrical double-layer capacitors, Angew. Chem. Int. Ed 51 (2012) 9994–10024.
[47] S.H. Aboutalebi, A.T. Chidembo, M. Salari, K. Konstantinov, D. Wexler, H.K. Liu, S.X. Dou, Comparison of GO, GO/MWCNTs composite and MWCNTs as potential electrode materials for supercapacitors, Energy Environ. Sci. 4 (2011) 1855–1865.
[48] C. Wang, D. Wu, H. Wang, Z. Gao, F. Xu, K. Jiang, Nitrogen-doped two-dimensional porous carbon sheets derived from clover biomass for high performance supercapacitors, J. Power Sour. 363 (2017) 375–383.
[49] G. Ma, F. Hua, K. Sunb, Z. Zhang, E. Feng, H. Peng, Z. Lei, Porous carbon derived from sorghum stalk for symmetric supercapacitors, RSC Adv. 6 (2016) 103508–103516.
[50] F. Ma, J. Wan, G. Wu, H. Zhao, Highly porous carbon microflakes derived from catkins for high-performance supercapacitors, RSC Adv. 5 (2015) 44416–44422.
[51] Q. Xie, A. Zheng, S. Zhai, S. Wu, C. Xie, Y. Zhang, Y. Guan, Reed straw derived active carbon/graphene hybrids as sustainable high-performance electrodes for advanced supercapacitors, J. Solid State Electrochem. 20 (2016) 449–457.
[52] N. Sudhan, K. Subramani, M. Karnan, N. Ilayaraja, M. Sathish, Biomass-derived activated porous carbon from rice straw for high-energy symmetric supercapacitor in aqueous and non-aqueous electrolytes, Energ Fuel 31 (2017) 977–985.
[53] S. Jiang, T. Shi, X. Zhan, H. Long, S. Xi, H. Hu, Z. Tang, High-performance all-solid-state flexible supercapacitors based on two-step activated carbon cloth, J. Power Sour. 272 (2014) 16–23.
[54] T. Wei, X. Wei, L. Yang, H. Xiao, Y. Gao, H. Li, A one-step moderate-explosion assisted carbonization strategy to sulfur and nitrogen dual-doped porous carbon nanosheets derived from camellia petals for energy storage, J. Power Sour. 331 (2016) 373–381.
[55] Y. Cheng, L. Huang, X. Xiao, B. Yao, L. Yuan, T. Li, Z. Hu, B. Wang, J. Wan, J. Zhou, Flexible and cross-linked N-doped carbon nanofiber network for high performance freestanding supercapacitor electrode, Nano Energy 15 (2015) 66–74.